The MUSIC Algorithm for Impedance Tomography of Small Inclusions from Discrete Data

A. Lechleiter*

June 8, 2015

Abstract

We consider a point-electrode model for electrical impedance tomography and show that current-to-voltage measurements from finitely many electrodes are sufficient to characterize the positions of a finite number of point-like inclusions. More precisely, we consider an asymptotic expansion with respect to the size of the small inclusions of the relative Neumann-to-Dirichlet operator in the framework of the point electrode model. This operator is naturally finite-dimensional and models difference measurements by finitely many small electrodes of the electric potential with and without the small inclusions. Moreover, its leading-order term explicitly characterizes the centers of the small inclusions if the (finite) number of point electrodes is large enough. This characterization is based on finite-dimensional test vectors and leads naturally to a MUSIC algorithm for imaging the inclusion centers. We show both feasibility and limitations of this imaging technique via two-dimensional numerical experiments, considering in particular the influence of the number of point electrodes on the algorithm's images.

1 Introduction

The Multiple Signal Classification (MUSIC) algorithm is a well-known technique to image small inclusions or obstacles in various settings. Starting with the pioneering work [Sch86], this algorithm has been applied to inverse scattering and inverse source problems [ML99, Dev00, AK04, Kir02, HR04, AIL05, Gri08], to electrical impedance tomography [BHV03, AGH07], and to inverse problems in elasticity [AKNT02, ACI08, GST12], to merely indicate some applications. While most of these papers consider the characterization of small objects in an infinite-dimensional setting by working in function spaces on a measurement surface, we propose an alternative in the context of impedance tomography working on finite-dimensional data gained by finitely many point electrodes. Arguably, results of this kind are somewhat natural, as the finite number of points to be characterized represents a finite-dimensional unknown, too. Our results are motivated

*Center for Industrial Mathematics, University of Bremen, Bremen, Germany

by corresponding theory in inverse scattering from [Kir02], see also [KG08, Section 4.1], where a finite number of far field measurements is used to characterize a finite number of point-like scatterers.

Despite measured data for any inverse problem is always finite-dimensional, quite few results on what can actually be characterized from finite datasets can be found in the literature. Thus, a first motivation of this paper is to show that in the framework of a point electrode model the positions of finitely many small inclusions can be rigorously characterized from finitely many difference measurements of the electric potential with and without inclusions. (The required number of measurements implicitly depends on the number of inclusions.) Due to an explicit range characterization via special test vectors, these inclusions can further be imaged with the help of the MUSIC algorithm, such that a second motivation is to numerically study the dependence of the resulting images on some parameters of the problem as, e.g., the number of point electrodes.

Our dimension-independent approach applies to the so-called point-electrode model of electrical impedance tomography (EIT), which can be considered as the limit case of the complete electrode model when the electrode size shrinks to zero, see [HHH11]. Given J inclusions in a connected domain $\Omega \subset \mathbb{R}^d$, $d = 2, 3$, that are scaled by a small parameter $\varepsilon > 0$ and centered at fixed points $\{z_1, \ldots, z_J\}$, we consider the difference of the Neumann-to-Dirichlet maps for the background conductivity and its perturbation by the J inclusions. If rescaled correctly, this difference, the so-called relative Neumann-to-Dirichlet operator, tends to a limit operator as ε tends to zero; this limit operator hence can be considered as a good measurement model for sufficiently small inclusions, see [CMV98, AK04, HS12].

When dealing with $N \in \mathbb{N}$ point electrodes, both the relative Neumann-to-Dirichlet operator and, upon rescaling, its limit $\mathbf{\Lambda}_N$ are symmetric matrices of size $N \times N$ that possess a one-dimensional kernel, i.e., the measured data is finite-dimensional and provides at most $N(N-1)/2$ degrees of freedom. The main result of the paper (see Theorem 6) shows that the matrix $\mathbf{\Lambda}_N$ characterizes the positions of the J small inclusions in the limit case as $\varepsilon \to 0$ via explicit test vectors $V_{z,\theta} \in \mathbb{R}^N$ for points $z \in \Omega$ and directions $\theta \in \mathbb{S}^{d-1} = \{x \in \mathbb{R}^d, |x|_2 = 1\}$: Roughly speaking, for N large enough there holds for all $z \in \Omega$ away from the boundary that

$$V_{z,\theta} \in \mathrm{Rg}(\mathbf{\Lambda}_N) \quad \Longleftrightarrow \quad z \in \{z_1, \ldots, z_J\}. \tag{1}$$

The MUSIC algorithm exploits this characterization for imaging the centers z_j by projecting the test vectors onto the kernel of (a noisy version of) $\mathbf{\Lambda}_N$ for points z in a grid covering Ω and then plotting the inverse of the norm of these projections on the grid points. The resulting plot indicates the positions of the inclusions, that is, the center points z_j, by strong peaks.

Our technique to prove (1) is motivated by [KG08, Section 4.1], where a similar problem has been considered for scattering from small acoustic scatterers. As in [KG08], a cornerstone of our analysis is a unique continuation argument, which implies that no estimate on the number of point electrodes required to characterize the positions of J small inclusions can be derived from our analysis. However, our numerical experiments

indicate rules of thumb on the required ratio between the number of electrodes and the number of inclusions such that the MUSIC algorithm works properly.

Let us finally note two important recent results on EIT in the framework of point electrode models: First, [HPS12, Sei14] prove that in two dimensions, roughly speaking, the knowledge of difference data for an infinite number of point electrodes characterizes the conductivity distribution entirely. A fundamental difference between their results and ours is that our analysis relies on the finite-dimensional leading-order term $\mathbf{\Lambda}_N$ of the relative Neumann-to-Dirichlet operator. As merely this leading-order term can be stably measured whenever the inclusions are small enough, results on what can be recovered from this limited dataset are of importance. In this regard, Theorem 6 shows that J inclusion centers are explicitly characterized by $\mathbf{\Lambda}_N$ if N is large enough compared to J.

Second, the recent paper [CHS14] constructively shows an interesting invisibility result for a setting similar to ours: For any fixed point electrode configuration, there always exists a conductivity different from the constant background conductivity that gives the same relative Neumann-to-Dirichlet data as the background conductivity. In contrast, we fix J point-like inclusions from the beginning and then vary the number of electrodes to characterize these inclusions.

Let us also note that the extension of our result to small inclusions with complex-valued or anisotropic material parameters or to impenetrable inclusions is straightforward, but will not be considered in this paper. It is also possible to generalize the setting to non-homogeneous background conductivities, at the expense of more involved technicalities to define (and to compute) the Neumann function. Moreover, our smoothness assumption that all domains are C^∞-smooth can be relaxed to, e.g., C^2-smoothness.

The structure of the rest of the paper is as follows: We introduce the setting that has already been sketched above in Section 2 and cite the necessary results on the asymptotics of the point electrode model in Section 3. That section also serves to define the finite-dimensional operators required for the characterization of the small inclusions in Section 4. Finally, we introduce and numerically test the MUSIC algorithm for EIT with point-electrode data in Section 5.

Notation: All vectors will be column vectors if nothing else is stated when defining them, and $(a;b)$ denotes the concatenation of two vectors $a \in \mathbb{R}^N$ and $b \in \mathbb{R}^M$ to a column vector in $\mathbb{R}^{N+M}$. By $|\cdot|_2$ and $|\cdot|_\infty$ we denote the Euclidean norm and the maximum norm on $\mathbb{R}^N$, respectively. Matrices are set in bold letters and the spectral norm of a matrix is denoted by $|\cdot|_2$ as well.

2 The Point Electrode Model for EIT

We consider static voltage potentials governed by the conductivity equation in a connected domain $\Omega \subset \mathbb{R}^d$, $d = 2, 3$, with C^∞-smooth boundary $\partial\Omega$. For a set $\{z_1, \dots, z_J\} \subset \Omega$ of $J \in \mathbb{N}$ pairwise disjoint points, a set of two-dimensional domains $D_j \subset \mathbb{R}^2$, $j = 1, \dots, J$, with smooth boundary such that each D_j contains the origin, and a scaling parameter $\varepsilon > 0$, we define

$$D_{j,\varepsilon} = z_j + \varepsilon D_j = \{y \in \mathbb{R}^2,\, (y - z_j)/\varepsilon \in D_j\} \subset \mathbb{R}^2.$$

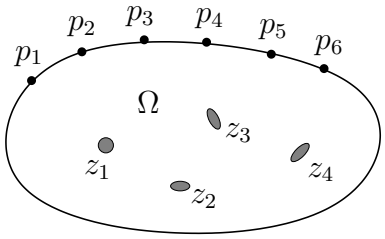

Figure 1: Sketch of the domain Ω containing $J = 4$ inclusions $\{z_1, \dots, z_4\}$ with $N = 6$ point electrodes $p_1, \dots, p_6$ on the boundary.

Further, we choose $\varepsilon_0 > 0$ such that for $0 < \varepsilon \leq \varepsilon_0$ all domains $D_{j,\varepsilon}$ are contained in Ω and pairwise disjoint. Hence, for $0 \leq \varepsilon < \varepsilon_0$,

$$D_\varepsilon = \bigcup_{j=1}^{J} D_{j,\varepsilon} \subset \Omega$$

is the union of J small inclusions contained in Ω. The conductivity in Ω equals

$$\sigma_\varepsilon = \begin{cases} 1 & \text{in } \Omega \setminus D_\varepsilon, \\ 1 + q_j & \text{in } D_{j,\varepsilon},\ j = 1, \dots, J, \end{cases} \qquad \text{with constants } q_j \neq 0 \text{ such that } q_j > -1. \quad (2)$$

We define ν to be the exterior unit normal field to Ω and, by abuse of notation, to each D_j, too. To each inclusion D_j we associate a polarization tensor $\boldsymbol{M}_{D_j,q_j} \in \mathbb{R}^{d\times d}$, explicitly given by

$$\boldsymbol{M}_{D_j,q_j} = \int_{\partial D_j} \nu \left(\frac{2+q_j}{2q_j} - K_{D_j} \right)^{-1} y^\top \, \mathrm{d}S(y),$$

where K_{D_j} is the double-layer operator for the Neumann function of Laplace's equation (see (5) and (24)), the inverse operator is applied component-wise to the row vector $y^\top$, and integration of the resulting matrix is done element-wise, see [HS12]. It is well-known that $\boldsymbol{M}_{D_j,q_j}$ is positive definite and thus invertible.

Consider a set of $N \geq 2$ disjoint points $p_1, \dots, p_N$ on the boundary of Ω that model the positions of infinitesimally small electrodes (see Figure 1 for a sketch), together with a current vector $I \in \mathbb{R}^N_\diamond = \{F \in \mathbb{R}^N, \sum_{n=1}^N F_n = 0\}$. (The sum of the injected currents vanishes due to conservation of charge.) Denote further by $\delta_{p_n} \in H^{(1-n)/2-\alpha}(\partial\Omega)$, $\alpha > 0$, the Dirac distribution supported at the nth point electrode p_n, defined by $\delta_{p_n}(v) = v(p_n)$ for $v \in C^0(\partial\Omega)$. In [HHR11] it is shown that the point electrode model

$$\operatorname{div}(\sigma_\varepsilon \nabla u) = 0 \quad \text{in } \Omega, \qquad \frac{\partial u}{\partial \nu} = \sum_{n=1}^{N} I_n \delta_{p_n} \quad \text{on } \partial\Omega, \qquad (3)$$

possesses a unique distributional solution u in the quotient space $H^{2-d/2-\alpha}(\Omega)/\mathbb{R}$ that satisfies the estimate $\|u\|_{H^{2-d/2-\alpha}(\Omega)/\mathbb{R}} \leq C(\alpha)|I|_2$ for arbitrary $\alpha > 0$. Further, [HHH11]

shows that the so-called complete electrode model approximates the point electrode model in (3) when N extended electrodes shrink to the N points $p_1, \dots, p_N$. Thus, this model is of practical relevance for EIT when small electrodes are considered.

The corresponding problem for the background conductivity $\gamma \equiv 1$,

$$\Delta u_0 = 0 \quad \text{in } \Omega, \qquad \frac{\partial u_0}{\partial \nu} = \sum_{n=1}^{N} I_n \delta_{p_n} \quad \text{on } \partial\Omega, \tag{4}$$

possesses a unique distributional solution u_0 in the quotient space $H^{2-d/2-\alpha}(\Omega)/\mathbb{R}$ as well, which is again bounded in terms of the current vector $I \in \mathbb{R}^N_\diamond$, i.e., $\|u\|_{H^{2-d/2-\alpha}(\Omega)/\mathbb{R}} \leq C(\alpha)|I|_2$. As the conductivity in (4) equals one, the solution u_0 can be explicitly expressed using the Neumann function $\mathcal{N}$ to Ω. For all $y \in \Omega$, this Green's function for Neumann boundary conditions satisfies

$$\Delta_x \mathcal{N}(\cdot, y) = -\delta_y \ \text{ in } \mathcal{D}'(\Omega), \quad \frac{\partial \mathcal{N}(\cdot, y)}{\partial \nu} = -\frac{1}{|\partial\Omega|} \ \text{ on } \partial\Omega \quad \text{and} \quad \int_{\partial\Omega} \mathcal{N}(\cdot, y)\, \mathrm{d}S = 0. \tag{5}$$

(The differential equation is satisfied in the distributional sense.) From [CK13] it follows that $\mathcal{N}(\cdot, y)$ is symmetric in its two arguments, that $\mathcal{N}(x, y) = \mathcal{N}(y, x)$ for $x \neq y$ in Ω and standard interior regularity theory for the Laplacian implies that $\mathcal{N}(\cdot, y)$ is infinitely differentiable in $\Omega \setminus \{y\}$. In particular, $\Phi_{\mathcal{N}}(\cdot, y) \in H^1(\Omega \setminus \overline{B_r(y)})$ for all $r > 0$ (but, as one can show, not for $r = 0$). By symmetry and smoothness, the Neumann function $\mathcal{N}$ can be extended to a continuous function in $\overline{\Omega} \times \overline{\Omega} \setminus \{(x, x),\, x \in \overline{\Omega}\}$. We finally note that [Sei11, Theorem 4.10] implies that the solution to (4) equals

$$u_0 = \sum_{j=1}^{N} \mathcal{N}(\cdot, p_n) I_n \qquad \text{in } \Omega. \tag{6}$$

To check this formula, note that $\int_{\partial\Omega} u_0 \, \mathrm{d}S = 0$ by definition of $\mathcal{N}$ (the trace is integrable over $\partial\Omega$.) In particular, the solution u_0 to (4) is smooth inside Ω.

Remark 1. *We denote the gradient of $\mathcal{N}$ with respect to the first variable by $\nabla_x \mathcal{N}$ while $\nabla_y \mathcal{N}$ is the gradient with respect to the second variable. Note that $\nabla_x \mathcal{N}(x, y) = \nabla_y \mathcal{N}(y, x)$ holds for $x \neq y \in \Omega$.*

3 Asymptotic Expansion of Potentials

Consider now the more general boundary value problem for the conductivity equation

$$\operatorname{div}(\sigma_\varepsilon \nabla u) = 0 \quad \text{in } \Omega, \qquad \frac{\partial u}{\partial \nu} = f \quad \text{on } \partial\Omega, \tag{7}$$

with Neumann boundary values $f \in H^s_\diamond(\partial\Omega) = \{f \in H^s(\partial\Omega), \langle f, \mathbf{1} \rangle = 0\}$, where $\mathbf{1}$ denotes the constant function equal to one everywhere, $\langle \cdot, \cdot \rangle$ denotes the duality product between $H^s(\partial\Omega)$ and $H^{-s}(\partial\Omega)$ for arbitrary $s \in \mathbb{R}$, and σ_ε has been defined in (2).

By elliptic regularity and duality arguments relying on the smoothness of $\partial\Omega$, each boundary datum $f \in H^s_\diamond(\partial\Omega)$ defines a unique solution $u \in H^{s+3/2}(\Omega)/\mathbb{R}$. We also introduce the corresponding Neumann problem for conductivity $\gamma \equiv 1$ and its solution in $H^{s+3/2}(\Omega)/\mathbb{R}$, that is again denoted by u_0,

$$\Delta u_0 = 0 \quad \text{in } \Omega, \qquad \frac{\partial u_0}{\partial \nu} = f \quad \text{on } \partial\Omega. \tag{8}$$

The Neumann-to-Dirichlet operator $\Lambda^{(\varepsilon)} : f \mapsto u|_{\partial\Omega}$, usually defined between the spaces $H^{-1/2}_\diamond(\partial\Omega)$ and $H^{1/2}(\partial\Omega)/\mathbb{R}$, extends to a bounded operator from $H^s_\diamond(\partial\Omega)$ into $H^{s+1}(\partial\Omega)/\mathbb{R}$. The analogous operator for background conductivity $\sigma \equiv 1$ is denoted by $\Lambda^{(0)}$. Since $\sigma_\varepsilon \equiv 1$ in some small neighborhood U of $\partial\Omega$ and since $u - u_0$ satisfies homogeneous Neumann boundary conditions on $\partial\Omega$, the difference $u - u_0$ is a smooth function in U by elliptic regularity results (see [HK11, Lemma 2.1] or the appendix of [HHR11]). An application of the trace theorem hence shows that $(u - u_0)|_{\partial\Omega}$ belongs to $H^r_\diamond(\partial\Omega)/\mathbb{R}$ for arbitrary $r \in \mathbb{R}$, and the estimate

$$\|u - u_0\|_{H^r(\partial\Omega)/\mathbb{R}} \leq C(r,s)\|f\|_{H^s(\partial\Omega)} \qquad \text{holds for arbitrary } r,\, s \in \mathbb{R}. \tag{9}$$

The relative Neumann-to-Dirichlet operator $\Lambda^{(\varepsilon)} - \Lambda^{(0)} : f \mapsto (u - u_0)|_{\partial\Omega}$ is hence bounded from $H^s_\diamond(\partial\Omega)$ into $H^r(\partial\Omega)/\mathbb{R}$ for arbitrary $r,\, s \in \mathbb{R}$.

Turning back to the above-introduced small inclusions $D_{j,\varepsilon}$, Theorem 3.6 in [HS12] shows the following expansion result.

Theorem 2 (Theorem 3.6 in [HS12])**.** *Let $f,\, g \in H^{-s}_\diamond(\partial\Omega)$ and denote by u_f and u_g the solution to* (8) *with boundary datum f and g, respectively. Then the expansion*

$$\langle g,\, (\Lambda^{(\varepsilon)} - \Lambda^{(0)})f\rangle = \varepsilon^d \sum_{j=1}^{J} \nabla u_g(z_j)^\top \boldsymbol{M}_{D_j,q_j} \nabla u_f(z_j) + \mathcal{O}(\varepsilon^{d+1}) \quad \text{as } \varepsilon \to 0$$

holds uniformly in f and $g \in H^{-s}_\diamond(\partial\Omega)$.

Restricting ourselves in the following to currents f of the form $\sum_{n=1}^N I_n \delta_{p_n}$ for $I \in \mathbb{R}^N_\diamond$, we assume to possess measurements of difference potentials at the same N point electrodes $p_1, \ldots, p_N$. These measurements define a finite-dimensional relative Neumann-to-Dirichlet map $(\boldsymbol{\Lambda}^{(\varepsilon)} - \boldsymbol{\Lambda}^{(0)})_N$ from $\mathbb{R}^N_\diamond$ into $\mathbb{R}^N/\mathbb{R}$: For $I = (I_1, \ldots I_N)^\top \in \mathbb{R}^N_\diamond$,

$$\left((\boldsymbol{\Lambda}^{(\varepsilon)} - \boldsymbol{\Lambda}^{(0)})_N I\right)_m = \left[\left(\Lambda^{(\varepsilon)} - \Lambda^{(0)}\right)\left(\sum_{n=1}^N I_n \delta_{p_n}\right)\right](p_m) \quad \text{for } 1 \leq m \leq N.$$

Theorem 2 transfers to this setting as follows.

Corollary 3. *Let I, I' be current vectors in $\mathbb{R}^N_\diamond$ and denote the unique solution to the conductivity problem* (4) *for current vector I and I' by u_I and $u_{I'} \in H^{2-d/2-\alpha}(\Omega)/\mathbb{R} \cap C^\infty(\Omega)$, respectively. Then the expansion*

$$I' \cdot (\boldsymbol{\Lambda}^{(\varepsilon)} - \boldsymbol{\Lambda}^{(0)})_N I = \varepsilon^d \sum_{j=1}^{J} \nabla u_{I'}(z_j)^\top \boldsymbol{M}_{D_j,q_j} \nabla u_I(z_j) + \mathcal{O}(\varepsilon^{d+1}) \quad \text{as } \varepsilon \to 0$$

holds uniformly in I and $I' \in \mathbb{R}^N_\diamond$.

Thus, for sufficiently small inclusions, difference measurements of the potentials u and u_0 for the same current vector $I \in \mathbb{R}^N_\diamond$ can be modeled with high accuracy by the scaled, finite-dimensional limit operator $\mathbf{\Lambda}_N$ of $(\mathbf{\Lambda}^{(\varepsilon)} - \mathbf{\Lambda}^{(0)})_N$,

$$I' \cdot (\mathbf{\Lambda}^{(\varepsilon)} - \mathbf{\Lambda}^{(0)})_N I \approx \varepsilon^d \, I' \cdot \mathbf{\Lambda}_N I \qquad \text{if } \varepsilon \ll 1, \tag{10}$$

where the linear mapping $\mathbf{\Lambda}_N : \mathbb{R}^N_\diamond \to \mathbb{R}^N/\mathbb{R}$ is defined by

$$I' \cdot \mathbf{\Lambda}_N I = \sum_{j=1}^{J} \nabla u_{I'}(z_j)^\top \boldsymbol{M}_{D_j,q_j} \nabla u_I(z_j) \qquad \text{for all } I' \in \mathbb{R}^N_\diamond. \tag{11}$$

To determine a matrix representation of $\mathbf{\Lambda}_N$ with respect to the standard basis of $\mathbb{R}^N$, we fix the mean value of $\mathbf{\Lambda}_N I \in \mathbb{R}^N/\mathbb{R}$ to be zero, such that $\mathbf{\Lambda}_N$ maps $\mathbb{R}^N_\diamond$ into $\mathbb{R}^N_\diamond$. For a given basis $I_1, \ldots, I_{N-1}$ of $\mathbb{R}^N_\diamond$ with entries $I_n = (I_{n,1}, \ldots, I_{n,N})^\top$ and corresponding solutions $u_1, \ldots, u_{N-1}$ to (4), the matrix representation of $\mathbf{\Lambda}_N$ with respect to this basis then factorizes into the matrices

$$\boldsymbol{H}_N := \begin{pmatrix} \nabla u_1(z_1) & \cdots & \nabla u_{N-1}(z_1) \\ \vdots & & \vdots \\ \nabla u_1(z_J) & \cdots & \nabla u_{N-1}(z_J) \end{pmatrix} \in \mathbb{R}^{dJ \times N-1},$$

and a block-diagonal matrix $\boldsymbol{M} \in \mathbb{R}^{dJ \times dJ}$ with $d \times d$ blocks on its diagonal containing the polarization tensors $\boldsymbol{M}_{D_j,q_j} \in \mathbb{R}^{d \times d}$,

$$\boldsymbol{M} = \begin{pmatrix} \boldsymbol{M}_{D_1,q_1} & & 0 \\ & \ddots & \\ 0 & & \boldsymbol{M}_{D_J,q_J} \end{pmatrix} \in \mathbb{R}^{dJ \times dJ}. \tag{12}$$

(When applying $\boldsymbol{M}$ to a vector $\phi \in \mathbb{R}^{dJ}$ we will write $\phi \in (\mathbb{R}^d)^J$ to emphasize that $\phi = (\phi_1; \ldots; \phi_J)$ contains J polarizations acting on the polarization tensors $\boldsymbol{M}_{D_j,q_j}$.) Indeed, (11) directly implies that the representation of $\mathbf{\Lambda}_N$ with respect to $I_1, \ldots, I_{N-1}$ reads $\boldsymbol{H}_N^\top \boldsymbol{M} \boldsymbol{H}_N$, because

$$(\boldsymbol{H}_N^\top \boldsymbol{M} \boldsymbol{H}_N)_{i,j} = \sum_{k=1}^{J} \nabla u_i(z_k)^\top \boldsymbol{M}_{(D_k,q_k)} \nabla u_j(z_k) \qquad \text{for } 1 \le i, j \le N-1.$$

In the sequel it will however be more convenient to deal with $\mathbf{\Lambda}_N$ as an operator mapping electrode currents in $\mathbb{R}^N_\diamond \subset \mathbb{R}^N$ to N electrode voltages, i.e., to represent $\mathbf{\Lambda}_N$ as an $N \times N$-matrix. To determine the matrix representation of $\mathbf{\Lambda}_N$ with respect to the standard basis of $\mathbb{R}^N$, consider again the basis $I_1, \ldots, I_{N-1}$ of $\mathbb{R}^N_\diamond$ with corresponding solutions $u_1, \ldots, u_{N-1}$ to (4). Define further $\boldsymbol{I}_N$ to be the $N \times N$-unit matrix and $I_N = (1, \ldots, 1)^\top \in \mathbb{R}^N$. As $I_1, \ldots, I_{N-1}, I_N$ is a basis of $\mathbb{R}^N$, the matrix $(I_1 \ \ldots \ I_{N-1} \ I_N) \in \mathbb{R}^{N \times N}$ is invertible and there is a unique matrix $\boldsymbol{B}_N \in \mathbb{R}^{N-1 \times N}$ and a unique vector $b \in \mathbb{R}^{n-1}$ that satisfy

$$\begin{pmatrix} \boldsymbol{B}_N \\ b^\top \end{pmatrix} \begin{pmatrix} I_1 & \ldots & I_{N-1} & I_N \end{pmatrix} = \boldsymbol{I}_N \quad \text{and} \quad \begin{pmatrix} I_1 & \ldots & I_{N-1} & I_N \end{pmatrix} \begin{pmatrix} \boldsymbol{B}_N \\ b^\top \end{pmatrix} = \boldsymbol{I}_N. \tag{13}$$

This implies that $b = (1/N, \dots, 1/N)^\top$, and hence $\boldsymbol{B}_N \begin{pmatrix} I_1 & \dots & I_{N-1} \end{pmatrix} = \boldsymbol{I}_{N-1}$. Note that $\mathrm{Ker}(\boldsymbol{B}_N) = \mathrm{span}\{b\} = \mathrm{Rg}(\boldsymbol{B}_N^\top)^\perp$, such that $\boldsymbol{B}_N^\top$ maps $\mathbb{R}^{N-1}$ into $\mathbb{R}^N_\diamond$. Due to (6), we further know that the entries of $\boldsymbol{H}_N$ can be represented as

$$\nabla u_k(z_j) = \nabla_x \sum_{n=1}^N \mathcal{N}(z_j, p_n) I_{k,n} = \sum_{n=1}^N \nabla_y \mathcal{N}(p_n, z_j) I_{k,n} \tag{14}$$

for $1 \le k \le N-1$ and $1 \le j \le J$. As $\boldsymbol{B}_N I$ yields the representation of a current vector $I \in \mathbb{R}^N_\diamond$ in the basis $I_1, \dots, I_N$ of $\mathbb{R}^N_\diamond$, the vector $\boldsymbol{H}_N \boldsymbol{B}_N I$ yields the current flow at the points z_j due to the current vector I. For a vector $\phi = (\phi_1; \dots; \phi_J) \in (\mathbb{R}^d)^J$, the matrix-vector product $\boldsymbol{B}_N^\top \boldsymbol{H}_N^\top \phi \in \mathbb{R}^N_\diamond$ on the other hand equals

$$\begin{aligned} \boldsymbol{B}_N^\top \boldsymbol{H}_N^\top \phi &= \boldsymbol{B}_N^\top \bigg(\sum_{j=1}^J \nabla u_k(z_j) \cdot \phi_j \bigg)_{k=1}^{N-1} = \boldsymbol{B}_N^\top \bigg(\sum_{j=1}^J \sum_{n=1}^N \nabla_y \mathcal{N}(p_n, z_j) \cdot \phi_j I_{k,n} \bigg)_{k=1}^{N-1} \\ &= \boldsymbol{B}_N^\top \bigg(I_k \cdot \bigg(\sum_{j=1}^J \nabla_y \mathcal{N}(p_n, z_j) \cdot \phi_j \bigg)_{n=1}^N \bigg)_{k=1}^{N-1} \\ &\overset{(13)}{=} \bigg(\sum_{j=1}^J \nabla_y \mathcal{N}(p_n, z_j) \cdot \phi_j - \frac{1}{N} \sum_{\ell=1}^N \sum_{j=1}^J \nabla_y \mathcal{N}(p_\ell, z_j) \cdot \phi_j \bigg)_{n=1}^N . \end{aligned} \tag{15}$$

Thus, the vector $\boldsymbol{B}_N^\top \boldsymbol{H}_N^\top \phi$ contains the point values of the potential $\sum_{j=1}^J \nabla u_k(z_j) \cdot \phi_j$ at the electrodes $p_1, \dots, p_N$, shifted by a constant such that their sum has mean-value zero. The matrix representation of $\boldsymbol{\Lambda}_N$ in the standard basis of $\mathbb{R}^n$ thus reads

$$\boldsymbol{\Lambda}_N = \boldsymbol{B}_N^\top \boldsymbol{H}_N^\top \boldsymbol{M} \boldsymbol{H}_N \boldsymbol{B}_N. \tag{16}$$

As $\boldsymbol{B}_N b = 0$, this representation indeed provides an $N \times N$ matrix mapping $\mathbb{R}^N_\diamond$ into $\mathbb{R}^N_\diamond$.

Theorem 4. *The ranges of $\boldsymbol{\Lambda}_N$ and $\boldsymbol{B}_N^\top \boldsymbol{H}_N^\top$ coincide.*

Proof. Since $\boldsymbol{M}$ is block-diagonal with symmetric and positive definite diagonal blocks $\boldsymbol{M}_{D_j, q_j} \in \mathbb{R}^{d \times d}$, there is a unique Cholesky decomposition $\boldsymbol{M} = \boldsymbol{G}^\top \boldsymbol{G}$ of $\boldsymbol{M}$ with an invertible matrix $\boldsymbol{G} \in \mathbb{R}^{dJ \times dJ}$. Setting $\boldsymbol{L} = \boldsymbol{G} \boldsymbol{H}_N \boldsymbol{B}_N$ implies by (16) that $\boldsymbol{\Lambda}_N = \boldsymbol{L}^\top \boldsymbol{L}$, such that $\mathrm{Rg}(\boldsymbol{\Lambda}_N) \subset \mathrm{Rg}(\boldsymbol{L}^\top) = \mathrm{Ker}(\boldsymbol{L})^\perp = \mathrm{Ker}(\boldsymbol{L}^\top \boldsymbol{L})^\perp = \mathrm{Ker}(\boldsymbol{\Lambda}_N)^\perp = \mathrm{Rg}(\boldsymbol{\Lambda}_N)$ due to symmetry of $\boldsymbol{\Lambda}_N$. All subspaces of $\mathbb{R}^N$ in this inclusion chain hence equal each other. Invertibility of $\boldsymbol{G}$ implies that $\mathrm{Rg}(\boldsymbol{L}^\top) = \mathrm{Rg}(\boldsymbol{B}_N^\top \boldsymbol{H}_N^\top)$, which implies the claim. □

4 Characterization of Small Inclusions

Our main theorem is going to characterize the range of $\boldsymbol{\Lambda}_N$ via suitable test vectors that we introduce next: For $z \in \Omega$ and $\theta \in \mathbb{S}^{d-1} = \{x \in \mathbb{R}^d,\ |x|_2 = 1\}$,

$$V_{z,\theta} := (\nabla_y \mathcal{N}(p_n, z) \cdot \theta)_{n=1}^N \in \mathbb{R}^N. \tag{17}$$

We further introduce the set $\overline{\Omega}_{\Gamma,\eta} := \{x \in \overline{\Omega},\, \mathrm{dist}(x,\Gamma) \geq \eta\}$ for an arbitrary parameter $\eta > 0$ and define the orthogonal projection $\mathbf{\Pi}_N$ onto vectors with mean value zero,

$$\mathbf{\Pi}_N : \mathbb{R}^N \to \mathbb{R}^N_\diamond \subset \mathbb{R}^N, \qquad \mathbf{\Pi}_N V = V - \frac{1}{N}\sum_{k=1}^N V_k.$$

Finally, fixing a sequence $(p_n)_{n\in\mathbb{N}} \subset \partial\Omega$ of pairwise distinct point electrodes on the boundary of Ω, the matrix $\mathbf{\Lambda}_N$ is from now on defined via the first N point electrodes $p_1, \ldots, p_N$ for arbitrary $N \geq 2$. The proof of our main theorem below relies on the following assumption.

Assumption 5. *The closure $\Gamma = \overline{\{p_n,\, n \in \mathbb{N}\}} \subset \partial\Omega$ has non-empty relative interior.*

Theorem 6 (Characterization of $\mathrm{Rg}(\mathbf{\Lambda}_N)$)**.** *If Assumption 5 holds, then for all $\eta > 0$ there is $N_0 \in \mathbb{N}$ such that for $z \in \overline{\Omega}_{\Gamma,\eta}$, arbitrary $\theta \in \mathbb{S}^{d-1}$, and all $N \geq N_0$ there holds*

$$z \in \{z_1, \ldots, z_J\} \quad \Longleftrightarrow \quad \mathbf{\Pi}_N V_{z,\theta} \in \mathrm{Rg}(\mathbf{\Lambda}_N).$$

Proof. If $z = z_k$ for some $k \in \{1, \ldots, J\}$, the representation of $\boldsymbol{H}_N$ shows that for $\phi = (\phi_1; \ldots; \phi_J)$ with $\phi_j = \delta_{j,k}\theta$ there holds

$$\begin{aligned}\boldsymbol{B}_N^\top \boldsymbol{H}_N^\top \phi &\overset{(15)}{=} \left(\sum_{j=1}^J \delta_{j,k} \nabla_y \mathcal{N}(p_n, z_j)\cdot\theta - \frac{1}{N}\sum_{n=1}^N\sum_{j=1}^J \delta_{j,k}\nabla_y\mathcal{N}(p_n,z_j)\cdot\theta\right)_{n=1}^N \\ &= \left(\nabla_x \mathcal{N}(p_n,z_k)\cdot\theta - \frac{1}{N}\sum_{n=1}^N \nabla_y\mathcal{N}(p_n,z_k)\cdot\theta\right)_{n=1}^N = \mathbf{\Pi}_N V_{z,\theta}.\end{aligned}$$

Thus, $\mathbf{\Pi}_N V_{z,\theta} \in \mathrm{Rg}(\boldsymbol{B}_N^\top \boldsymbol{H}_N^\top)$. In the subsequent Lemmas 8 and 9 we further prove that there is $N_0 = N_0(J,\eta)$, such that for $N \geq N_0$ and $z \in \overline{\Omega}_{\Gamma,\eta} \setminus \{z_1, \ldots, z_J\}$ the projection $\mathbf{\Pi}_N V_{z,\theta}$ does not belong to $\mathrm{Rg}(\boldsymbol{B}_N^\top \boldsymbol{H}_N^\top)$. The claim of the theorem then follows from Theorem 4, stating that the ranges of $\mathbf{\Lambda}_N$ and $\boldsymbol{B}_N^\top \boldsymbol{H}_N^\top$ coincide if N is large enough. □

The following auxiliary lemma will be convenient to prove Lemmas 8 and 9.

Lemma 7. *Assume that Assumption 5 holds and choose any finite set of M pairwise distinct points $z^{(1)}, \ldots, z^{(M)} \in \overline{\Omega} \setminus \Gamma$. Then there is $N_0 \in \mathbb{N}$ such that for all $N \geq N_0$ the dipole potential $v = \sum_{j=1}^M \nabla_y \mathcal{N}(\cdot, z^{(j)})\cdot\phi_j$ with $\phi = (\phi_1; \ldots; \phi_M) \in (\mathbb{R}^d)^M$ is constant on the point electrodes $p_1, \ldots, p_N$ if and only if $\phi = 0$.*

Proof. We argue by contradiction, exploiting the unique continuation principle.

(1) Assume that for arbitrarily large $N \in \mathbb{N}$ there is $\phi^N = (\phi_1^N; \ldots; \phi_M^N) \in (\mathbb{R}^d)^M$ such that the indicated dipole potential is constant on the set $\{p_n,\, 1 \leq n \leq N\}$, i.e.,

$$v_N(p_n) = \sum_{j=1}^M \nabla_y \mathcal{N}(p_n, z^{(j)})\cdot\phi_j^N = c_N \quad \text{for some } c_N \in \mathbb{R}.$$

We divide this equation by the maximum norm of ϕ^N and, for simplicity, denote the normalized vector again by ϕ^N and the constant on the right again by c_N. Due to normalization, we can then extract a convergent subsequence of the vectors $(\phi^N)_{N\in\mathbb{N}} \subset (\mathbb{R}^d)^M$ that we denote, by abuse of notation, again by $(\phi^N)_{N\in\mathbb{N}}$: $\phi^N \to \phi \in (\mathbb{R}^d)^M$ as $N\to\infty$ and $|\phi|_\infty = |\phi^N|_\infty = 1$ by continuity of the norm. The corresponding pointwise limit of v_N equals

$$v(x) := \sum_{j=1}^J \nabla_y \mathcal{N}(x, z_j)\cdot\phi_j, \qquad x\in\overline{\Omega}\setminus\bigcup_{j=1}^J\{z_j\}. \tag{18}$$

As v_N takes a constant value at all points p_n, $1\le n\le N$, there is $c\in\mathbb{R}$ such that $v(p_n)=c$ for all $n\in\mathbb{N}$. (Clearly, c equals the limit of the c_N.)

(2) The continuity of v in a neighborhood of $\partial\Omega$ implies that v is constant on the closure Γ of the points $\{p_n,\, n\in\mathbb{N}\}\subset\partial\Omega$ and, due to Assumption 5, the relative interior of Γ in $\partial\Omega$ is non-empty. Since the normal derivative of $\mathcal{N}(\cdot,z)$ is constant on $\partial\Omega$ and independent of $z\in\Omega$, the normal derivative of both components of $\nabla_y\mathcal{N}(\cdot,z)$ vanishes on Γ for all $z\in\Omega$. Thus, the normal derivative of v vanishes on Γ, too, and the unique continuation property for solutions to Laplace's equation implies that $v=c$ is constant in $\Omega\setminus\bigcup_{j=1}^J\{z_j\}$. Consequently, the singularity of $\nabla_y\mathcal{N}(\cdot,z_j)$ at z_j implies that $\phi_j=0$ for all j, i.e., $\phi=0$. This contradicts the fact that $|\phi|_\infty=1$, such that our initial assumption was wrong. For arbitrary pairwise distinct points $z^{(1)},\dots,z^{(M)}$ there is hence a minimal number $N_0\in\mathbb{N}$ of point electrodes such that the dipole potential v from (18) is constant at $p_1,\dots,p_{N_0}$ if and only if $\phi=(\phi_1;\dots;\phi_M)$ vanishes. □

The next lemma treats points in $\overline{\Omega}_{\Gamma,\eta}$, defined after (17), that are far from all centers.

Lemma 8. *If Assumption 5 holds, then for all $\eta>0$ there is $N_0\in\mathbb{N}$ such that for all $z\in\overline{\Omega}_{\Gamma,\eta}\setminus\bigcup_{j=1}^J B(z_j,\eta)$ and all $\theta\in\mathbb{S}^{d-1}$, the projection $\boldsymbol{\Pi}_N V_{z,\theta}$ does not belong to the range of $\boldsymbol{B}_N^\top\boldsymbol{H}_N^\top$.*

Proof. (1) We argue again by contradiction and consider, in a preparatory step, the matrix-valued function

$$\boldsymbol{K}_N(z) := \boldsymbol{B}_N^\top \begin{pmatrix} \nabla u_1(z_1)^\top & \dots & \nabla u_1(z_J)^\top & \nabla u_1(z)^\top \\ \vdots & & \vdots & \vdots \\ \nabla u_{N-1}(z_1)^\top & \dots & \nabla u_{N-1}(z_J)^\top & \nabla u_{N-1}(z)^\top \end{pmatrix} \in \mathbb{R}^{N\times d(J+1)}$$

for points in $z\in\overline{\Omega}\setminus(\{z_1,\dots,z_J\}\cup\Gamma)$ that neither belong to the centers z_j nor to the closure of the point electrodes.

If $\boldsymbol{K}_N(z)\phi$ vanishes for some non-zero $\phi=(\phi_1;\dots;\phi_{J+1})\in(\mathbb{R}^d)^{J+1}$, then the dipole potential $v=\sum_{j=1}^J\nabla_y\mathcal{N}(\cdot,z^{(j)})\cdot\phi_j+\nabla_y\mathcal{N}(\cdot,z)\cdot\phi_{J+1}$ takes a constant value at all point electrodes $p_1,\dots p_N$ due to the construction of $\boldsymbol{B}_N$. Thus, Lemma 7 shows that for every $z\in\overline{\Omega}\setminus(\{z_1,\dots,z_J\}\cup\Gamma)$ there is $N_0(z)$ such that $\boldsymbol{K}_N(z)$ is injective for all $N\ge N_0(z)$. In other words, the nullity $\operatorname{null}\boldsymbol{K}_N(z) := \dim\operatorname{Ker}\boldsymbol{K}_N(z)$ satisfies $\operatorname{null}\boldsymbol{K}_N(z)=0$ for $N\ge N_0(z)$.

The mapping $z \mapsto \boldsymbol{K}_N(z)$ depends continuously on $z \in \overline{\Omega} \setminus \Gamma$, because each potential u_n is continuous in $\overline{\Omega} \setminus \Gamma$ due to (14). As the dimension of the null space of a matrix is moreover an upper semicontinuous function of the matrix entries, the composition $z \mapsto \operatorname{null} \boldsymbol{K}_N(z)$ is upper semicontinuous in $\overline{\Omega} \setminus \Gamma$, too, i.e.,

$$\text{if } z^{(k)} \to z \text{ in } \overline{\Omega} \setminus \Gamma \text{ then } \limsup_{k\to\infty} \operatorname{null} \boldsymbol{K}_N(z^{(k)}) \le \operatorname{null} \boldsymbol{K}_N(z).$$

Consequently, for any $z \in \overline{\Omega} \setminus \Gamma$ there is $r(z) > 0$ such that $\operatorname{null} \boldsymbol{K}_N(z') \le \operatorname{null} \boldsymbol{K}_N(z)$ holds for all z' in $U(z) := B(z, r(z)) \cap [\overline{\Omega} \setminus \Gamma]$. As the nullity is decreasing in N, there holds for all $z \in \overline{\Omega} \setminus (\{z_1, \dots, z_J\} \cup \Gamma)$ and all $z' \in U(z)$ that $\operatorname{null} \boldsymbol{K}_N(z') \le \operatorname{null} \boldsymbol{K}_{N_0}(z) = 0$ for all $N \ge N_0(z)$.

For arbitrary $\eta > 0$, the union $\{z' \in U(z),\, z \in \overline{\Omega} \setminus (\{z_1, \dots, z_J\} \cup \Gamma)\}$ of relatively open sets covers the compact set $\overline{\Omega}_{\Gamma,\eta} \setminus \bigcup_{j=1}^J B(z_j, \eta)$ from the claim, such that $\overline{\Omega}_{\Gamma,\eta} \subset \bigcup_{j=1}^L U(z^{(j)})$ for points $z^{(1)}, \dots, z^{(L)}$ in $\overline{\Omega} \setminus (\{z_1, \dots, z_J\} \cup \Gamma)$. Setting $N_0 := \max_{j=1,\dots,L} N_0(z^{(j)})$ hence implies that $N_0(z) \le N_0$ for all $z \in \overline{\Omega}_{\Gamma,\eta}$ and choosing $N \ge N_0$ shows that $\boldsymbol{K}_N(z)$ is injective for all $z \in \overline{\Omega}_{\Gamma,\eta}$.

(2) Assume, for contradiction, that $\boldsymbol{B}_N^\top \boldsymbol{H}_N^\top \phi = \boldsymbol{\Pi}_N V_{z,\theta}$ for some $N \ge N_0$, $z \in \overline{\Omega}_{\Gamma,\eta} \setminus \bigcup_{j=1}^J B(z_j, \eta)$, $\theta \in \mathbb{S}^{d-1}$, and $\phi = (\phi_1; \dots; \phi_J) \in (\mathbb{R}^d)^J$. As in (15), one shows that

$$\begin{aligned}\boldsymbol{\Pi}_N V_{z,\theta} &= \left(\nabla_y \mathcal{N}(p_n, z) \cdot \theta - \frac{1}{N} \sum_{\ell=1}^N \nabla_y \mathcal{N}(p_n, z) \cdot \theta \right)_{n=1}^N \\ &= \boldsymbol{B}_N^\top \left(I_k \cdot \left(\nabla_y \mathcal{N}(p_n, z) \cdot \theta \right)_{n=1}^N \right)_{k=1}^{N-1} = \boldsymbol{B}_N^\top \big(\nabla u_k(z) \cdot \theta \big)_{k=1}^{N-1},\end{aligned}$$

and, due to the representation of $\boldsymbol{H}_N$, our assumption $\boldsymbol{B}_N^\top \boldsymbol{H}_N^\top \phi = \boldsymbol{\Pi}_N V_{z,\theta}$ implies that the matrix-vector product of $\boldsymbol{K}_N(z)$ and $(\phi_1; \dots; \phi_J; -\theta) \in \mathbb{R}^{d(J+1)}$ vanishes. Thus, $(\phi_1; \dots; \phi_J; -\theta) \in (\mathbb{R}^d)^{J+1}$ must vanish because $\boldsymbol{K}_N(z)$ is injective due to the first part of this proof, which is impossible as $|\theta|_2 = 1$. □

Lemma 9. *If Assumption 5 holds, then there are $\eta > 0$ and $N_0 \in \mathbb{N}$ such that $\boldsymbol{\Pi}_N V_{z,\theta}$ does not belong to the range of $\boldsymbol{B}_N^\top \boldsymbol{H}_N^\top$ for all $N \ge N_0$, all $z \in \bigcup_{j=1}^J [\overline{B(z_j, \eta)} \setminus \{z_j\}]$ and all $\theta \in \mathbb{S}^{d-1}$.*

Proof. (1) Assume, on the contrary, that there are vectors $(\phi^N)_{N\in\mathbb{N}} \subset (\mathbb{R}^d)^J$, points $(z_N)_{N\in\mathbb{N}} \subset \bigcup_{j=1}^J [\overline{B(z_j, \eta)} \setminus \{z_j\}]$, and directions $(\theta_N)_{N\in\mathbb{N}} \subset \mathbb{S}^{d-1}$ such that

$$\boldsymbol{B}_N^\top \boldsymbol{H}_N^\top \phi^N = \boldsymbol{\Pi}_N V_{z_N,\theta_N} \quad \text{holds for arbitrarily large } N \in \mathbb{N}. \tag{19}$$

(To simplify notation, we assume (19) to hold even for all $N \in \mathbb{N}$.) By construction of $\boldsymbol{B}_N$, $\boldsymbol{H}_N$, and V_{z_N,θ_N}, (19) implies that $v_N := \sum_{j=1}^J \nabla_y \mathcal{N}(\cdot, z_j) \cdot \phi_j^N$ satisfies

$$v_N(p_n) = \sum_{j=1}^J \nabla_y \mathcal{N}(p_n, z_j) \cdot \phi_j^N = \nabla_y \mathcal{N}(p_n, z_N) \cdot \theta_N + c_N, \quad n = 1, \dots, N, \tag{20}$$

for some sequence $(c_N)_{N\in\mathbb{N}} \subset \mathbb{R}$.

(2) The norms $|\phi^N|_\infty$ are uniformly bounded in N, because the maximum norm of $V_{z_N,\theta_N} \in \mathbb{R}^N_\diamond$ is also uniformly bounded. To prove this statement, assume that $|\phi^N|_\infty$ grows over all bounds as $N \to \infty$. Divide (19) by $|\phi^N|_\infty$ and extract a convergent subsequence of $\phi^N/|\phi^N|_\infty$ with non-trivial limit $0 \neq \phi = (\phi_1; \ldots; \phi_J) \in (\mathbb{R}^d)^J$. Since $\mathbf{\Pi}_N V_{z_N,\theta_N}/|\phi^N|_\infty$ tends to zero as $N \to \infty$, one shows as in the second part of the proof of Lemma 8 that $v(x) := \sum_{j=1}^J \nabla_y \mathcal{N}(x, z_j) \cdot \phi_j$ is constant on Γ. Lemma 7 hence implies that ϕ must vanish, which is a contradiction. Thus, $(\phi^N)_{N\in\mathbb{N}} \subset (\mathbb{R}^d)^J$ is bounded.

(3) Due to the boundedness of the vectors $\phi^N \in (\mathbb{R}^d)^J$ we can extract a convergent subsequence with limit $\phi \in (\mathbb{R}^d)^J$, and, by abuse of notation, denote that subsequence again by $(\phi^N)_{N\in\mathbb{N}}$. Proceeding in the same way with the points $(z_N)_{\ell\in\mathbb{N}}$ and the directions $(\theta_N)_{\ell\in\mathbb{N}}$ yields convergent sequences $(z_N)_{N\in\mathbb{N}}$ with limit $z \in \bigcup_{j=1}^J \overline{B(z_j, \eta)}$ and $(\theta_N)_{N\in\mathbb{N}}$ with limit $\theta \in \mathbb{S}^{d-1}$, respectively.

If the limit point z does not equal one of the centers z_j, we can directly pass to the limit in (20) and conclude by Lemma 7 that both $\phi \in (\mathbb{R}^d)^J$ and the limiting direction θ must vanish, which is a contradiction as $\theta \in \mathbb{S}^{d-1}$. Thus, z_N must tend to a center z_k for some $k \in \{1, \ldots, N\}$, and taking the limit as $N \to \infty$ in (20) shows that

$$\sum_{1\le j\neq k\le J} [\nabla_y \mathcal{N}(p_n, z_j) \cdot \phi_j] + \nabla_y \mathcal{N}(p_n, z_k) \cdot \phi_k - \nabla_y \mathcal{N}(p_n, z_k) \cdot \theta = c, \qquad n \in \mathbb{N},$$

where c is the limit of the constants c_N. Thus, Lemma 7 implies that $\phi_j = 0$ for $1 \le j \neq k \le J$ and $\phi_k = \theta$. Fixing $n \in \{1, \ldots, N\}$, we rewrite (20) as

$$\sum_{1\le j\neq k\le J} \nabla_y \mathcal{N}(p_n, z_j) \cdot \phi_j^N + \nabla_y \mathcal{N}(p_n, z_k) \cdot (\phi_k^N - \theta_N) + \big[\nabla_y \mathcal{N}(p_n, z_k) - \nabla_y \mathcal{N}(p_n, z_N)\big] \cdot \theta_N = c_N. \quad (21)$$

Because $z \mapsto \nabla_y \mathcal{N}(p_n, z) \cdot \theta$ is continuously differentiable in Ω, the mean value theorem implies existence of $\xi_n^N \in [z_k, z_N] := \{tz_N + (1-t)z_k,\, t \in [0,1]\}$ such that

$$[\nabla_y \mathcal{N}(p_n, z_k) - \nabla_y \mathcal{N}(p_n, z_N)] \cdot \theta_N = \theta_N \cdot \nabla_y^2 \mathcal{N}(p_n, \xi_n^N)(z_k - z_N); \quad (22)$$

here $\nabla_y^2 \mathcal{N}(p_n, \xi_n^N) \in \mathbb{R}^{d\times d}$ is the Hessian of $\mathcal{N}$ at (p_n, ξ_n^N) with respect to the second variable. First rewriting (21) by inserting (22) and then dividing by $d_N := \sum_{j\neq k} |\phi_j^N|_\infty + |\phi_k^N - \theta_N|_\infty + |z_k - z_N|_\infty > 0$ shows that

$$\sum_{1\le j\neq k\le J} \nabla_y \mathcal{N}(p_n, z_j) \cdot \frac{\phi_j^N}{d_N} + \nabla_y \mathcal{N}(p_n, z_k) \cdot \frac{\phi_k^N - \theta_N}{d_N} + \theta_N \cdot \nabla_y^2 \mathcal{N}(p_n, \xi_n^N) \frac{z_k - z_N}{d_N} = \frac{c_N}{d_N}.$$

By definition of d_N, all fractions on the left of the last equation are bounded by one, either in the maximum norm or in absolute value. Thus, we can extract convergent subsequences of ϕ_j^N/d_N, $(\phi_k^N - \theta_N)/d_N$, and $(z_k - z_N)/d_N$ with limits $\hat\phi_j \in \mathbb{R}^d$, $\hat\theta \in \mathbb{R}^d$ and $\hat z \in \mathbb{R}^2$ independent of $n \in \mathbb{N}$. At least one of these limits must be non-trivial

because $\sum_{j\neq k} |\phi_j^N|_\infty/d_N + |\phi_k^N - \theta_N|_\infty/d_N + |z_k - z_N|_\infty/d_N = 1$. As $\xi_n^N \in [z_k, z_N]$ tends to z_k as $N \to \infty$,

$$\sum_{1\leq j\neq k\leq J} \nabla_y \mathcal{N}(p_n, z_j)\cdot\hat{\phi}_j + \nabla_y \mathcal{N}(p_n, z_k)\cdot\hat{\theta} + \theta\cdot\nabla_y^2\mathcal{N}(p_n, z_k)\hat{z} = c \quad \text{for all } n\in\mathbb{N}.$$

As in the proof of Theorem 7, this implies that the multipole

$$x \mapsto \sum_{1\leq j\neq k\leq J} \nabla_y \mathcal{N}(x, z_j)\cdot\hat{\phi}_j + \nabla_y \mathcal{N}(x, z_k)\cdot\hat{\theta} + \theta\cdot\nabla_y^2\mathcal{N}(x, z_k)\hat{z}$$

is constant in $\Omega\setminus\{z_1,\dots,z_k\}$. Due to the singularities of the latter function at the centers z_j and the different order of singularity of the dipole $x\mapsto\nabla_y\mathcal{N}(x,z_k)\cdot\hat{\theta}$ and the quadrupole $x\mapsto\theta\cdot\nabla_y^2\mathcal{N}(x,z_k)\hat{z}$, this is only possible if $\hat{\phi} = (\hat{\phi}_1;\dots;\hat{\phi}_J)$, $\hat{\theta}$, and $\hat{z}$ vanish. (Note that $\theta\in\mathbb{S}^{d-1}$ cannot vanish.) However, we argued above that at least one of these quantities must be non-trivial, such that our initial assumption of the proof was wrong, proving the lemma's statement. □

5 The MUSIC Algorithm

Theorem 6 states that if $N\in\mathbb{N}$ is large enough, then $\boldsymbol{\Pi}_N V_{z,\theta}\in\mathbb{R}^N_\diamond$ belongs to the range of $\boldsymbol{\Lambda}_N$ if and only if $z\in\overline{\Omega}_{\Gamma,\eta}$ is one of the centers $\{z_1,\dots,z_J\}$ of the J small inclusions. This motivates the basic idea of the MUSIC algorithm: The norm of the orthogonal projection of $\boldsymbol{\Pi}_N V_{z,\theta}$ onto the null space of $\boldsymbol{\Lambda}_N$ is an indicator function that peaks precisely at the centers $\{z_1,\dots,z_J\}$.

A crucial tool for the implementation of the MUSIC algorithm is the singular value decomposition $\boldsymbol{\Lambda}_N = \boldsymbol{U}\boldsymbol{D}\boldsymbol{V}^\top$ factorizing $\boldsymbol{\Lambda}_N$ into a diagonal matrix $\boldsymbol{D}\in\mathbb{R}^{N\times N}$ containing the singular values $(\sigma_j)_{j=1}^N\subset\mathbb{R}_{\geq 0}$ of $\boldsymbol{\Lambda}_N$ in decreasing order and orthogonal matrices $\boldsymbol{U}$ and $\boldsymbol{V}$ in $\mathbb{R}^{N\times N}$ containing the corresponding left- and right singular vectors $(u_j)_{j=1}^N$ and $(v_j)_{j=1}^N\subset\mathbb{R}^N$ in their columns, respectively. Note that Corollary 3 implies that J small inclusions in Ω lead to precisely dJ non-zero singular values $\sigma_1,\dots,\sigma_{dJ}$.

As measured data is always contaminated by instrumental noise, and as voltage difference measurements provide approximations to $(\boldsymbol{\Lambda}^{(\varepsilon)} - \boldsymbol{\Lambda}^{(0)})_N$ instead of $\boldsymbol{\Lambda}_N$, the exact matrix $\boldsymbol{\Lambda}_N$ is never at hand in practice. We hence assume to possess measurements $(\boldsymbol{\Lambda}^{(\varepsilon)} - \boldsymbol{\Lambda}^{(0)})_N^\delta\in\mathbb{R}^{N\times N}$ that satisfy $|(\boldsymbol{\Lambda}^{(\varepsilon)} - \boldsymbol{\Lambda}^{(0)})_N^\delta - (\boldsymbol{\Lambda}^{(\varepsilon)} - \boldsymbol{\Lambda}^{(0)})_N|_2 \leq \delta|(\boldsymbol{\Lambda}^{(\varepsilon)} - \boldsymbol{\Lambda}^{(0)})_N|_2$ for some relative noise level $\delta > 0$. The corresponding singular value decomposition is $(\boldsymbol{\Lambda}^{(\varepsilon)} - \boldsymbol{\Lambda}^{(0)})_N^\delta = \boldsymbol{U}^\delta\boldsymbol{D}^\delta(\boldsymbol{V}^\delta)^\top$ with singular values $(\sigma_j^\delta)_{j=1}^N\subset\mathbb{R}_{\geq 0}$ and singular vectors $(u_j^\delta)_{j=1}^N$ and $(v_j^\delta)_{j=1}^N\subset\mathbb{R}^N$. Perturbation theory for the singular value decomposition [Ste06, Li98] shows that if $\varepsilon\ll 1$ and $\delta\ll 1$ are sufficiently small, then the singular values $(\sigma_j^\delta)_{j=1}^N$ are close to those of $\varepsilon^d\boldsymbol{\Lambda}_N$ and the orthogonal projections $\boldsymbol{P}V := \sum_{j=1}^{dJ}[V\cdot u_j]u_j$ and $\boldsymbol{P}^\delta V := \sum_{j=1}^{dJ}[V\cdot u_j^\delta]u_j^\delta$ onto the singular subspace spanned by the largest dJ right singular vectors are close as well. This allows in particular to identify the number of inclusions from the singular values of $(\boldsymbol{\Lambda}^{(\varepsilon)} - \boldsymbol{\Lambda}^{(0)})_N^\delta$, as the largest dJ singular values of $(\boldsymbol{\Lambda}^{(\varepsilon)} - \boldsymbol{\Lambda}^{(0)})_N$ all have a magnitude of about $\varepsilon^d|\boldsymbol{\Lambda}_N|_2$ whereas σ_{dJ+1}^δ is about a factor of ε smaller.

In its simplest form, the MUSIC-algorithm uses the projection $\boldsymbol{P}^\delta$ to project the test function $\boldsymbol{\Pi}_N V_{z,\theta}$ onto the orthogonal complement of $\operatorname{span}\{u_1^\delta, \dots, u_{dJ}^\delta\}$ and plots the indicator function

$$z \mapsto \frac{1}{|(\boldsymbol{I}_N - \boldsymbol{P}_\delta)\boldsymbol{\Pi}_N V_{z,\theta}|_2} \tag{23}$$

on a grid of points z inside Ω for some fixed $\theta \in \mathbb{S}^{d-1}$. If N is large enough and both the inclusion size ε and the noise level $\delta \ll 1$ are small enough, then this indicator shows strong peaks at the center points $z_1, \dots, z_J$ of the inclusions. Various improved or adapted variants exist, see, e.g., [ML99, BHV03], but will not be discussed here.

We demonstrate feasibility, performance, and limitations of the MUSIC algorithm for dimension $d = 2$ and the unit disc $\Omega = \{x \in \mathbb{R}^2,\ |x|_2 < 1\}$, such that

$$\mathcal{N}(x,y) = \begin{cases} -\frac{1}{2\pi}\left[\log|x-y|_2 + \log\left(\left||x|y|_2 - \frac{y}{|y|_2}\right|_2\right)\right] & \text{for } x \neq y \in \Omega,\ y \neq 0, \\ -\frac{1}{2\pi}\log|x|_2 & \text{for } x \in \Omega \setminus \{0\},\ y = 0, \end{cases} \tag{24}$$

is the explicitly known Neumann function. In Ω, we consider four circular inclusions $D_{j,\varepsilon} = \{x \in \mathbb{R}^2,\ |x - z_j|_2 \leq \varepsilon\}$ for $j = 1, \dots, 4$ with centers $z_1 = (-0.45, -0.35)^\top$, $z_2 = (-0.45, 0.45)^\top$, $z_3 = (0.45, 0.05)^\top$, and $z_4 = (0.20, -0.45)^\top$. We choose the radius ε of these circles among the three values 0.1, 0.05, and 0.02. All contrasts q_j equal -0.8 and we choose 32 equidistant points on the boundary $\partial\Omega$ as point electrodes, see Figure 2(a). To compute numerical approximations to $(\boldsymbol{\Lambda}^{(\varepsilon)} - \boldsymbol{\Lambda}^{(0)})_{32}$ we use the finite element software FreeFem++ (see [Hec12]) and directly approximate $(\boldsymbol{\Lambda}^{(\varepsilon)} - \boldsymbol{\Lambda}^{(0)})_{32} I_n$ for a basis $I_1, \dots, I_{31}$ of $\mathbb{R}^{32}_\diamond$ via a single source problem for the corresponding difference potential. (The current vectors are chosen as sine and cosine patterns.) Figures 2(b)–(d) show the 31 non-zero singular values (marked by filled dots) of numerical approximations to $(\boldsymbol{\Lambda}^{(\varepsilon)} - \boldsymbol{\Lambda}^{(0)})_{32}$ for the three radii under consideration. The theoretically predicted gap between the eighth and ninth singular value of $\boldsymbol{\Lambda}_{32}$ is visible in the singular spectrum of $(\boldsymbol{\Lambda}^{(\varepsilon)} - \boldsymbol{\Lambda}^{(0)})_{32}$ for all three radii, such that the correct number of inclusions can in each case be deduced from the singular values of these non-perturbed matrices. Figures 2(b)–(d) also show the *perturbed* singular values of $(\boldsymbol{\Lambda}^{(\varepsilon)} - \boldsymbol{\Lambda}^{(0)})^\delta_{32}$ for relative noise levels δ equal to 0.001, 0.01, and 0.05. While for $\delta = 0.001$ there is a significant gap between the eighth and ninth perturbed singular value, this gap reduces when increasing the noise level. For $\delta = 0.05$, the seventh and eighth singular value is strongly affected by the artificial noise, such that the resulting images are likely to have low quality. Apart from this, the relative noise level of five percent is clearly too high to deduce the correct number of inclusions from the perturbed singular values.

In our numerical experiments, it turned out to considerably improve the resolution of the resulting images if instead of choosing a fixed dipole direction $\theta \in \mathbb{S}^1$ one minimizes the right-hand side of (23) over several directions. Algorithmically, we do so by computing the corresponding indicators for $M = 10$ equidistant directions in the set $\Theta_M = \{(\cos(2\pi\ell/M), \sin(2\pi\ell/M))^\top,\ \ell = 1, \dots, M\} \subset \mathbb{S}^1$. We hence set

$$\mathcal{I}_N^\delta(z) = \frac{1}{\min_{\theta\in\Theta_M} |(\boldsymbol{I}_N - \boldsymbol{P}_\delta)\boldsymbol{\Pi}_N V_{z,\theta}|_2} \tag{25}$$

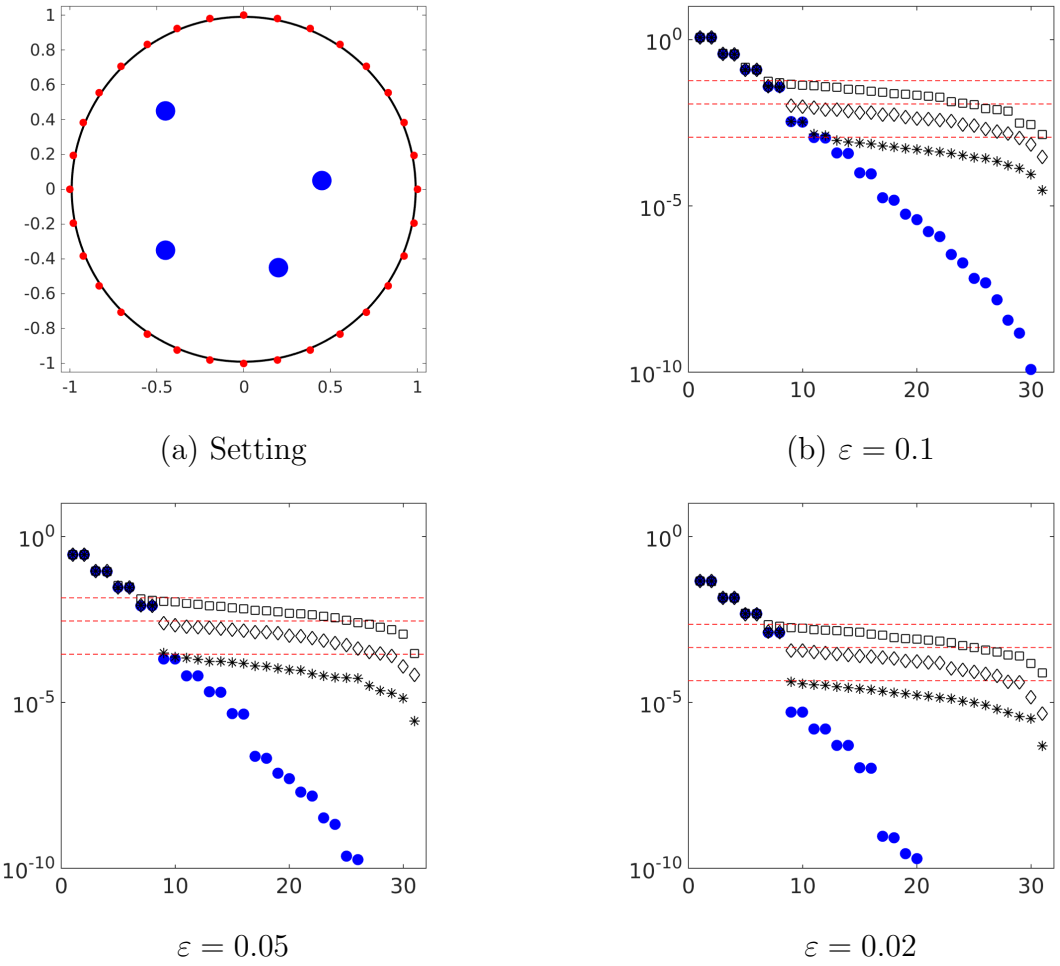

Figure 2: (a) Positions of the four inclusions with radius 0.05 in the unit circle. Dots mark the 32 point electrodes. (b)–(d) Singular values of $(\mathbf{\Lambda}^{(\varepsilon)} - \mathbf{\Lambda}^{(0)})_{32}$ for $\varepsilon = 0.1$, 0.05, and 0.02 in (b), (c), and (d), marked by filled dots. In each plot, stars, diamonds and squares mark the corresponding perturbed singular values for noise levels $\delta = 0.001$, 0.01, and 0.05. Singular values less than 10^{-10} and not plotted and horizontal lines indicate the relative noise levels.

This modified indicator function is efficiently implemented in two dimensions via matrix-vector multiplications since the corresponding arrays easily fit into the memory of a standard desktop computer, such that optimization algorithms can be avoided. Even if further increasing M is cheap, this number turned out to be sufficient to guarantee a sufficient level of directional independence of the reconstructions, as Figure 3 indicates. (The evaluation of $\mathcal{I}_N^\delta$ with $M = 10$ at about 31.400 points takes less than 1.5 seconds on a single core of an Intel i5 processor (4 cores, 3.2 GHz) using MATLAB, once the test vectors are precomputed.)

Figure 4 shows the indicator $z \mapsto \mathcal{I}_N^\delta(z)$ from (25) for radii 0.02, 0.5, and 0.1 and relative noise levels 0.001, 0.01, and 0.05. The images for $\delta = 0.001$ all peak at the

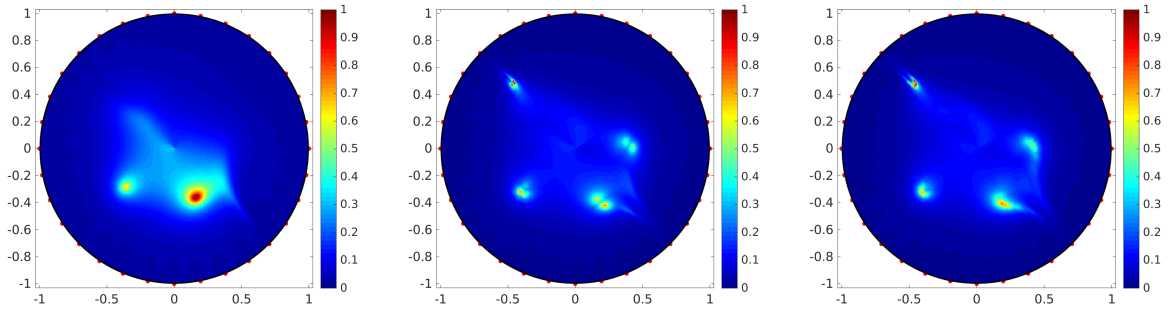

(a) $M = 1$ (b) $M = 4$ (c) $M = 10$

Figure 3: The modified indicator $\mathcal{I}_{32}^{\delta}$ from (25) for $M = 1, 4$, and 10 in (a), (b), and (c). Fixed parameters are $\varepsilon = 0.02$ and $\delta = 10^{-8}$.

inclusion centers and, arguably, are of the same quality; for $\delta = 0.01$, all indicators all lose contrast compared to the smaller noise level. Further, several elongated artifacts towards the electrodes become more pronounced compared to the images for $\delta = 0.001$; they seem to a be a particular feature of the algorithm in the framework of the point electrode model. Increasing δ to 0.05 yields images where none of the four inclusions is anymore detectable; interestingly the resulting plots however still take small values outside the convex hull of the small inclusions. By carefully checking the plots for $\delta = 0.001$ or 0.01 one notes that their peaks, i.e., their local maxima, are slightly shifted towards to center of the circular domain when compared to the true inclusion centers, except for the top right inclusion.

We next explore limitations of the MUSIC algorithm with respect to the number N of point electrodes and fix the radius of the inclusions from now on to $\varepsilon = 0.02$. In a first step, we reduce N from 32 to 16 by omitting every second point electrode. Figure 5 plots the exact singular values of $(\mathbf{\Lambda}^{(\varepsilon)} - \mathbf{\Lambda}^{(0)})_N$ for $\varepsilon = 0.02$ and $N = 16$, as well as their perturbations for noise levels 0.001, 0.01, and 0.05. The same comments on the perturbation of the first $dJ = 8$ singular values as in Figure 2(d) apply. However, the reduction of N from 32 to 16 implies a reduction from 15 to 7 of the dimension of the singular subspace linked to those singular values $\sigma_{dJ+1}^{\delta}, \ldots, \sigma_{N-1}^{\delta}$ corresponding to the kernel of $\mathbf{\Lambda}_N$. Since the MUSIC algorithm relies on the orthogonal projection onto this so-called noise subspace, its dimension is as crucial for the algorithm as the dimension of the subspace linked to the largest dJ singular values. Figures 5(b) and (c) show that for noise levels 0.001 and 0.01 the MUSIC algorithm is still able to peak at roughly the correct positions of the inclusions. For $\delta = 0.01$, the image quality reduces to about the same level as in Figure 4(d), with arguably slightly extended artifacts towards the point electrodes, such that a noise subspace of dimension seven still provides reasonable images of four inclusions. However, further reducing the number of electrodes to $N = 12$ results in a drastic decrease of image quality, as the noise subspace is merely three-dimensional anymore. This low dimension implies that the indicator function depends significantly on the added artificial noise, which is not the case for the previously considered examples.

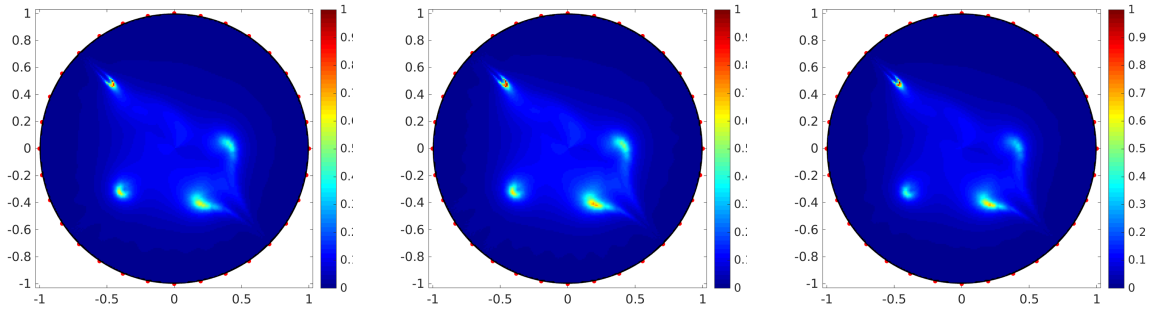

(a) $\varepsilon = 0.02$, $\delta = 0.001$ (b) $\varepsilon = 0.05$, $\delta = 0.001$ (c) $\varepsilon = 0.1$, $\delta = 0.001$

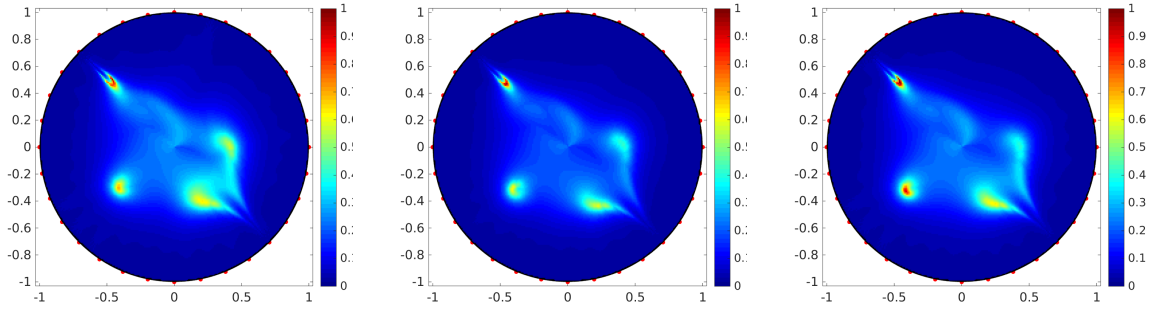

(d) $\varepsilon = 0.02$, $\delta = 0.01$ (e) $\varepsilon = 0.05$, $\delta = 0.01$ (f) $\varepsilon = 0.1$, $\delta = 0.01$

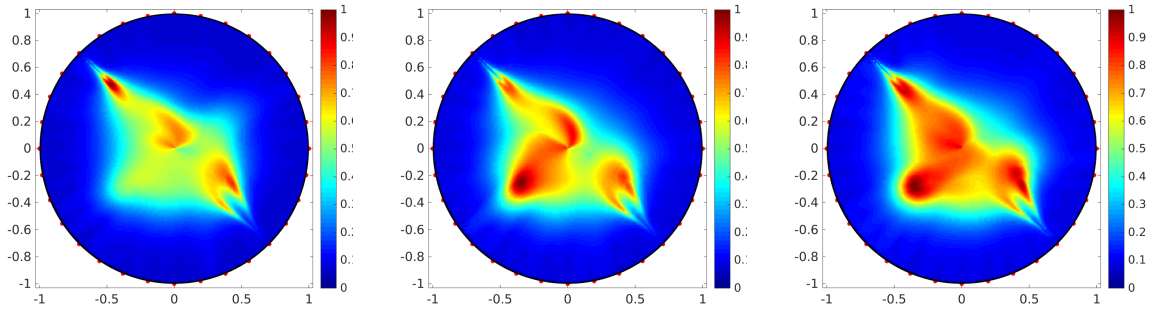

(g) $\varepsilon = 0.02$, $\delta = 0.05$ (h) $\varepsilon = 0.05$, $\delta = 0.05$ (i) $\varepsilon = 0.1$, $\delta = 0.05$

Figure 4: Indicator $\mathcal{I}_{32}^{\delta}$ for different radii ε and different relative noise levels δ. For plots in the left column ε equals 0.2, and $\varepsilon = 0.05$ and 0.1 for the middle and right column, respectively. The top row corresponds to $\delta = 0.001$, the middle row to $\delta = 0.01$, and the bottom row to $\delta = 0.05$.

Figures 5(e) and (f) show representative indicators for noise levels $\delta = 0.001$ and 0.01 that do neither allow to deduce the correct number of inclusions nor their positions.

If one keeps the $N = 12$ point electrodes fixed but reduces the number of inclusions to $J = 3$ by omitting the top right one centered at z_4, the number of singular values of size ε reduces to 6, such that the noise subspace becomes five-dimensional. In this setting, the indicator function $\mathcal{I}_{12}^{\delta}$ from (25) is again able to identify the positions of the three inclusions at least roughly, see Figures 5(h) and (i). Due to artifacts close to the

peaks at the inclusion centers it is however difficult to precisely estimate these centers for the relative noise level $\delta = 0.01$, see Figure 5(i).

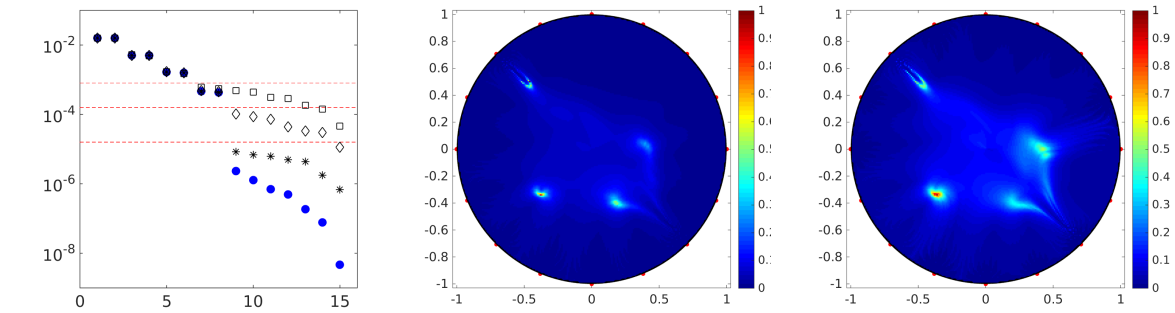

(a) Singular values ($N = 16$) (b) $\delta = 0.001$ (c) $\delta = 0.01$

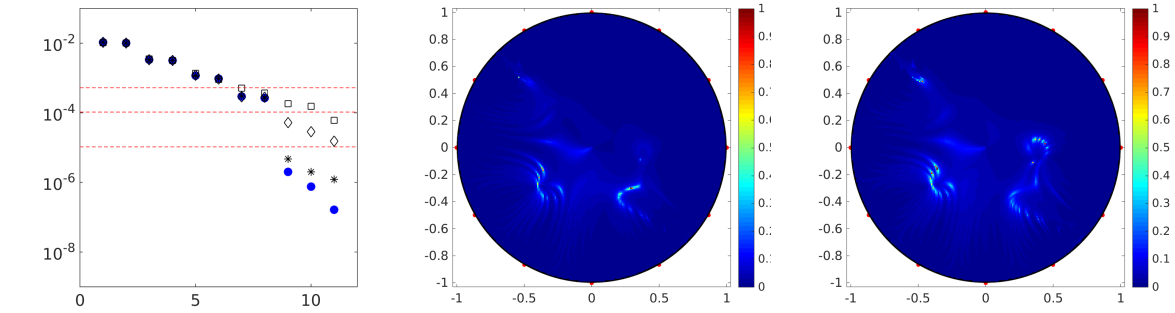

(d) Singular values ($N = 12$) (e) $\delta = 0.001$ (f) $\delta = 0.01$

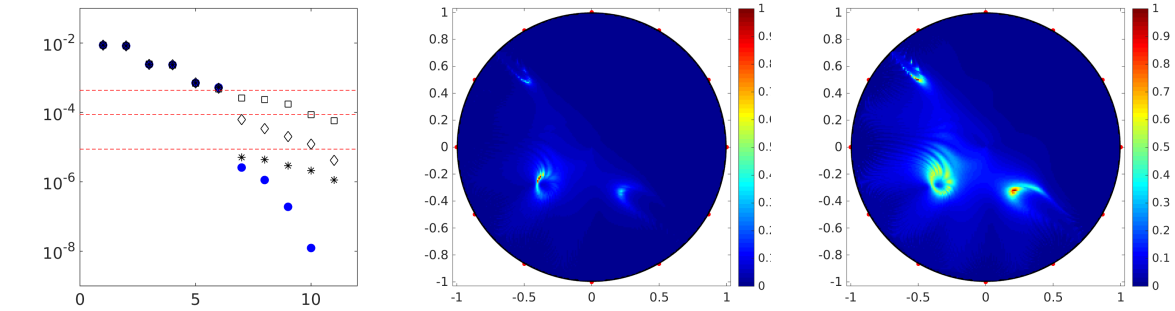

(g) Sing. val. ($J = 3$, $N = 12$) (h) $\delta = 0.001$ (i) $\delta = 0.01$

Figure 5: (a) Filled dots mark singular values of $(\mathbf{\Lambda}^{(0.02)} - \mathbf{\Lambda}^{(0)})_{16}$, i.e., $N = 16$ and $\varepsilon = 0.02$; perturbed singular values are marked by stars ($\delta = 0.001$), diamonds ($\delta = 0.01$), and squares ($\delta = 0.05$). (b)–(c) Indicator $\mathcal{I}^{\delta}_{16}$ for relative noise levels $\delta = 0.001$ and 0.01. (d) Filled dots mark singular values of $(\mathbf{\Lambda}^{(0.02)} - \mathbf{\Lambda}^{(0)})_{12}$, i.e., $N = 12$; perturbed singular values are marked as in (a). (e)–(f) Indicator $\mathcal{I}^{\delta}_{12}$ for $\delta = 0.001$ and 0.01. (g) Filled dots mark singular values of $(\mathbf{\Lambda}^{(0.02)} - \mathbf{\Lambda}^{(0)})_{12}$ when only three inclusions are present (the top right one is omitted); perturbed singular values are marked as in (a). (h)–(i) Indicator $\mathcal{I}^{\delta}_{12}$ computed from the data $(\mathbf{\Lambda}^{(0.02)} - \mathbf{\Lambda}^{(0)})_{12}$ from (g) for $\delta = 0.001$ and 0.01.

Let us finally summarize the presented numerical experiments by two conclusions

on the required number of electrodes: If the dimension of the noise subspace as well as the number of inclusions can clearly be identified from the singular values of the data matrix, then a clear indication that the number of point electrodes is sufficiently large to correctly image the inclusions is that the dimension of the noise subspace is at least about the number of inclusions. If these subspaces are not clearly identifiable, then either the size of the inclusions or the noise level might be too large to obtain clear pictures from the indicator function $\mathcal{I}_N^\delta$ in (25). In this situation, according to our experiments, a good test for any guess of the number of inclusions is whether the indicator function $\mathcal{I}_N^\delta$ shows stable peaks under small random perturbations of the data matrix.

Acknowledgements

The author would like to thank the anonymous referees for various remarks leading to substantial improvements of the paper.

References

[ACI08] H. Ammari, P. Calmon, and E. Iakovleva. Direct elastic imaging of a small inclusion. *SIAM J. Imaging Sci.*, 1:169–187, 2008.

[AGH07] H. Ammari, R. Griesmaier, and M. Hanke. Identification of small inhomogeneities: Asymptotic factorization. *Math. Comp.*, 76(259):1425–1449, 2007.

[AIL05] H. Ammari, E. Iakovleva, and D. Lesselier. A MUSIC algorithm for locating small inclusions buried in a half-space from the scattering amplitude at a fixed frequency. *Multiscale Model. Simul.*, 3:597–628, 2005.

[AK04] H. Ammari and H. Kang. *Reconstruction of Small Inhomogeneities From Boundary Measurements*, volume 1846 of *Lecture Notes in Mathematics*. Springer, 2004.

[AKNT02] H. Ammari, H. Kang, G. Nakamura, and K. Tanuma. Complete asymptotic expansions of solutions of the system of elastostatics in the presence of an inclusion of small diameter and detection of an inclusion. *J. Elasticity*, 67:97–129, 2002.

[BHV03] M. Brühl, M. Hanke, and M. Vogelius. A direct impedance tomography algorithm for locating small inhomogeneities. *Numer. Math.*, 93:635–654, 2003.

[CHS14] L. Chesnel, N. Hyvönen, and S. Staboulis. Construction of invisible conductivity perturbations for the point electrode model in electrical impedance tomography. *ArXiv e-prints*, December 2014.

[CK13] J. Choi and S. Kim. Neumann functions for second order elliptic systems with measurable coefficients. *Trans. Amer. Math. Soc.*, 2013.

[CMV98] D. J. Cedio-Fengya, S. Moskow, and M. S. Vogelius. Identification of conductivity imperfections of small diameter by boundary measurements. continuous dependence and computational reconstruction. *Inverse Probl.*, 14(3):553, 1998.

[Dev00] A.J. Devaney. Super-resolution processing of multi-static data using time reversal and MUSIC. Preprint, 2000.

[Gri08] R. Griesmaier. An asymptotic factorization method for inverse electromagnetic scattering in layered media. *SIAM J. Appl. Math.*, 68:1378–1403, 2008.

[GST12] D. Gintides, M. Sini, and N. T. Thành. Detection of point-like scatterers using one type of scattered elastic waves. *Journal of Computational and Applied Mathematics*, 236:2137–2145, 2012.

[Hec12] F. Hecht. New development in FreeFem++. *J. Numer. Math.*, 20:251–265, 2012.

[HHH11] M. Hanke, B. Harrach, and N. Hyvönen. Justification of point electrode models in electrical impedance tomography. *Math. Models Methods Appl. Sci.*, 21:1395–1413, 2011.

[HHR11] M. Hanke, N. Hyvönen, and S. Reusswig. Convex backscattering support in electric impedance tomography. *Numer. Math.*, 117:373–396, 2011.

[HK11] M. Hanke and A. Kirsch. Sampling methods. In O. Scherzer, editor, *Handbook of Mathematical Methods in Imaging*, chapter 12. Springer, New York, 2011.

[HPS12] N. Hyvönen, P. Piiroinen, and O. Seiskari. Point measurements for a Neumann-to-Dirichlet map and the Calderón problem in the plane. *SIAM J. Math. Anal.*, 44:3526–3536, 2012.

[HR04] C. Hazard and K. Ramdani. Selective acoustic focusing using time-harmonic reversal mirrors. *SIAM J. Appl. Math.*, 64(3):1057–1076, 2004.

[HS12] N. Hyvönen and O. Seiskari. Detection of multiple inclusions from sweep data of electrical impedance tomography. *Inverse Probl.*, 28:095014, 2012.

[KG08] A. Kirsch and N. I. Grinberg. *The Factorization Method for Inverse Problems*. Oxford Lecture Series in Mathematics and its Applications 36. Oxford University Press, 2008.

[Kir02] A. Kirsch. The MUSIC-algorithm and the factorization method in inverse scattering theory for inhomogeneous media. *Inverse Problems*, 18:1025–1040, 2002.

[Li98] R.-C. Li. Relative perturbation theory: II. Eigenspace and singular subspace variations. *SIAM. J. Matrix Anal. & Appl.*, 20(2):471–492, 1998.

[ML99] J. Mosher and R. Leahy. Source localization using recursively applied and projected (RAP) MUSIC. *IEEE Transactions on Signal Processing*, 47:332–340, 1999.

[Sch86] R. Schmidt. Multiple emitter location and signal parameter estimation. *IEEE Transactions on Antennas and Propagation*, 34(3):276–280, Mar 1986.

[Sei11] O. Seiskari. Locating multiple inclusions from sweep data of electrical impedance tomography. Master's thesis, Aalto University, 2011.

[Sei14] O. Seiskari. Point electrode problems in piecewise smooth plane domains. *SIAM J. Math. Anal.*, 46:1204–1227, 2014.

[Ste06] M. Stewart. Perturbation of the SVD in the presence of small singular values. *Linear Algebra and its Applications*, 419:53–77, 2006.